JMEPEG (2011) 20:1520–1535
DOI: 10.1007/s11665-011-9844-0

1059-9495/$19.00

Comparative Discrete-Particle Versus Continuum-Based Computational Investigation of Soil Response to Impulse Loading

M. Grujicic, B. Pandurangan, and A. Hariharan

(Submitted November 14, 2010)

Two representative soil models are compared and contrasted within two transient nonlinear dynamics computational analyses. The first soil model is representative of a discrete-particle group of models, while the other is a typical continuum-type consolidated-soil model. The two computational analyses involved: (a) the case of a soil slug impacting a rigid flat surface and (b) the case of detonation of a mine shallow buried in soil and the interaction of the resulting gaseous detonation products, mine fragments, and soil ejecta with a plate-like deformable steel target. The results obtained show that the use of the computationally more expensive particle mechanics-based soil models is fully justified only in the case of loose (low-density) soil. In addition, the magnitude of the particle-to-particle coefficient of restitution has been found to have a second-order effect on the extent of momentum transferred from the moving soil to the target and that it may be substantially different from its effective counterpart for the entire loose-soil agglomerate.

Keywords blast loading, CU-ARL, detonation of shallow-buried mines, discrete-particle soil model

1. Introduction

Recent experience of the U.S. military forces in Afghanistan and Iraq clearly showed that buried and ground-laid landmines are a major threat to the survivability of lightweight vehicles (such as the Light Tactical Vehicle) and their occupants. The observed destructive power of detonated landmines is the result of the large impulsive loads brought about by the incident blast/shock waves and by the impact of mine casing fragments and soil ejecta. It is, hence, no surprise that the design and development of military vehicles (and general structural platforms) with a high-level of blast survivability entails the ability to understand and quantify the impulsive loads associated with the detonation of landmines [of different shapes, sizes, and depth-of-burial (DOB)] deployed in different soil media and to model the kinematic/structural response of the targeted platforms. In general, however, the elucidation and quantification of the (time-dependent) loads (experienced by the targeted structure) resulting from the detonation a buried landmine is quite challenging since such loads depend strongly on the size and shape of the charge, its depth of burial, the distance between the soil surface and the target, and the properties (density, particle size and distribution, presence of inorganic/organic matter, water content, etc.) of the soil in which the landmine is buried. Direct experimental characterizations of landmine-blast events are highly critical for getting a better understanding of the accompanying highly complex phenomena. However, it is not practical or cost-effective to carry out experimental determination of the response of all targets of interest to buried charges of all sizes in a variety of soils. Recent advances in numerical analysis capabilities, particularly the coupling of Eulerian solvers (used to model gaseous detonation products and air) and Lagrangian solvers (used to represent vehicles/platforms and soil), have allowed simulations to provide insight into complex loading created by the mine blast event. However, a quantified understanding of the blast phenomena and loadings through computer modeling is still not mature. As discussed in our previous work (Ref 1), the lack of maturity of computer simulations of the blast event is mainly due to inability of the currently available materials models to realistically represent the response of the materials involved under large deformation, high-deformation rate, high-temperature conditions, the type of conditions accompanying landmine detonation. In particular, the soil response and its dependence on the soil composition, microstructure, and water content are poorly understood (Ref 2).

A review of the literature carried out as part of the present work shows that there exists an extensive body of work dealing with the investigation of detonation of buried charges. However, a detailed examination of such work reveals that the main focus of this work is not on the elucidation of blast phenomena and characterization of landmine blast output or on the survivability of structures subjected to blasts (Ref 3), but rather on the investigation of soil cratering processes (with applications toward the efficient utilization of explosives for excavation).

Among the work published in the open literature, which directly deals with experimental characterization of the effects of the detonation of buried landmine, the following appear to be the most relevant to the present subject matter: (a) Westine et al. (Ref 4) carried out experiments on a plate which was mounted

M. Grujicic, B. Pandurangan, and **A. Hariharan**, Department of Mechanical Engineering, Clemson University, 241 Engineering Innovation Building, Clemson, SC 29634-0921. Contact e-mail: gmica@clemson.edu.

above a buried charge representing an antitank landmine. The plate contained a number of through-the-thickness holes at incremental distances from the mine, in which, plugs of known mass were placed. The blast accompanying mine detonation caused the plugs to be driven out of the holes and from their velocity the impulsive loading on the plate was calculated; (b) Morris (Ref 5) used the results of Westine et al. (Ref 4), to construct a design-for-survivability computer code for light-weight vehicles; (c) Bergeron et al. (Ref 6) carried out a comprehensive investigation of the buried landmine blasts using an instrumented ballistic pendulum. From these experiments, the pressure and impulse as a function of time were recorded at several locations in air directly above the mine as well as in the sand surrounding the mine, along with x-radiographs and high-speed photographs of the associated soil cratering and ejecting phenomena; and (d) Braid (Ref 7) subsequently extended the work of Bergeron et al. (Ref 6) by incorporating different charge sizes, soil types and improved instrumentation.

As mentioned above, material models generally used to describe the behavior of soil under blast loading conditions suffer from a number of short-comings all related to the inability of these models to account properly for the effect of soil microstructure, composition, degree of compaction, and hydration level on its physical response. To overcome these short-comings, Clemson University and the Army Research Laboratory (ARL), Aberdeen, Proving Ground, MD jointly developed and subsequently parameterized [using the results of a detailed investigation of dynamic response of soil at different saturation levels, as carried out by researchers at the Cavendish Laboratory, Cambridge, UK (Ref 8, 9)] a new so-called "CU-ARL" soil model (Ref 10-13). This model is capable of capturing the effects of: (a) soil average particle size and particle size distribution; (b) the initial level of compaction/density; (c) clay, silt, and gravel contents; and (d) degree of soil saturation with water. The model was validated (Ref 14-17) against a series of experimental data such as the one associated with: (a) the aforementioned experimental investigation of Bergeron and Tremblay (Ref 2); (b) the experimental investigation of Bergeron et al. (Ref 6) involving a mine impulse pendulum; (c) experimental investigation of Foedinger (Ref 18) involving high-speed photographs of the soil-overburden bubble formation, burst and soil-ejection/cratering as well as pressure measurements within the soil and air; and (d) temporal evolution of the transmitted impulse as measured using the vertical impulse measurement fixture (VIMF) in the work of Skaggs et al. (Ref 19). The CU-ARL soil model was subsequently used in a series of computational investigations dealing with the assessment of vehicle survivability to blast loading, a trade-off between vehicle up-armoring and its off-road performance and the extent and type of injuries experienced by the targeted-vehicle occupants (Ref 20-23).

The aforementioned CU-ARL soil model is an example of the continuum-type material model, within which the granular nature of the soil is taken into account only indirectly (through proper formulation and parameterization of the material constitutive relations). Recently, however, there has been a lot of work being done on modeling soil as a truly granular material comprised an assembly of discrete soil particles (e.g., Ref 24, 25). While majority of recent efforts have been focused on the specific issues related to the behavior of a granular medium (e.g., inter-particle contact detection, normal and tangential contact properties, etc.), there have been efforts also aimed at formulating a material model suitable for use in computational analysis of impulse loading by soil-overburden and soil-ejecta impacts (e.g., Ref 26). It is generally argued that these models, due to the fact that they account explicitly for granular nature of the soil, must be intrinsically more accurate. What is generally neglected to consider is the fact that many aspects of particle mechanics-based soil models are founded on ad hoc laws and concepts (due to the lack of knowledge of the underlying physical phenomena). Nevertheless, what can be expected, in general, is that discrete-particle models should be more appropriate, than their continuum counterparts, in the low-density soil regime. As will be discussed in greater detail in next section, this regime is generally found in the propelled soil over-burden bubble as well as in the loose-soil ejecta (particularly in the case of dry soil with low-level of particle adhesion).

The main objective of the present work is to carry out a comparison in the computational predictions based on two soil models: (a) CU-ARL soil model and (b) the discrete-particle soil model by Deshpande et al. (Ref 26). The main question to be answered is how much difference in the soil kinematic/structural response is observed under identical impulse loading conditions, depending on which soil model is used.

The organization of the article is as follows. A brief overview of the main temporal phases and spatial zones, within the soil associated with detonation of a mine buried in soil is presented in section 2. The discrete-particle soil model developed by Deshpande et al. (Ref 26) is overviewed in section 3. The CU-ARL continuum-type soil model (Ref 10-13) is summarized in section 4. Details regarding the problem definition, formulation of the finite element analysis and associated results pertaining to the cases of a soil slug impacting a rigid flat surface and detonation of a shallow-buried mine are presented, respectively, in sections 5 and 6. The main conclusions resulting from the present work are summarized in section 7.

2. Detonation of Shallow-Buried and Ground-Laid Mines

Detonation of explosives is a chemical reaction which, at very high rate, converts initially solid (or liquid) explosive into a high-pressure, high-temperature expanding gas. Expansion of the gaseous detonation product(s) is accompanied by balance of various energies (thermal, potential, kinetic, strain, etc.). In principle, in the case of landmines, buried in soil or ground laid, one may distinguish between two limiting situations:

(a) The so-called "camouflet" scenario in which the mine is buried quite deep into the ground. Consequently, mine detonation leads merely to the conversion of the detonation-product potential energy into surface energy of fractured soil particles, and inelastic and elastic strain energy of the soil. In this case, gaseous detonation products are trapped under the ground and, due to extensive attenuation of the soil-borne shocks, no significant shock is transmitted into the air above the soil. Thus, this type of detonation does not introduce any threat to a target structure located at or above the ground;
(b) Detonation of the ground-laid mines which typically result in a very small energy transfer into the underlying

soil. In this case, the main threat to an above-the-ground target structure arises from the kinetic energy of the detonation products and the impulse energy carried by airborne shock waves.

In the majority of situations, mines are shallow buried in soil and the main threat to the target structure arises from the soil ejecta which, due to their large kinetic energy, can transfer significant portion of the momentum to the target. Since this regime of mine deployment, is of main concern to the designers of blast-survivable structures (e.g., vehicle hull), it is examined in greater detail in the remainder of this section.

In the time domain, detonation of landmines shallow buried in soil can be divided into three well-defined phases, Fig. 1(a)-(f):

(a) The initial phase within which high-pressure, high-temperature expanding gaseous detonation products interact with the surrounding soil. Typically, three distinct soil zones can be identified. Typical size of each of these zones scales with the mine characteristic dimension (e.g., radius, R_e). The three zones can be characterized as: (i) Within the inner most zone, the "zone of crushing" which extends ca. $2R_e - 3R_e$, the attendant pressures and temperatures are so high that the material constitutive response is of little influence; (ii) In a zone which extends between ca. $3R_e$ and $6R_e$, the soil undergoes shock-induced deformation by irreversible compaction and fracture/crushing of the soil particles; and (iii) The outermost zone which extends beyond ca. $6R_e$ and within which shock propagation leads to

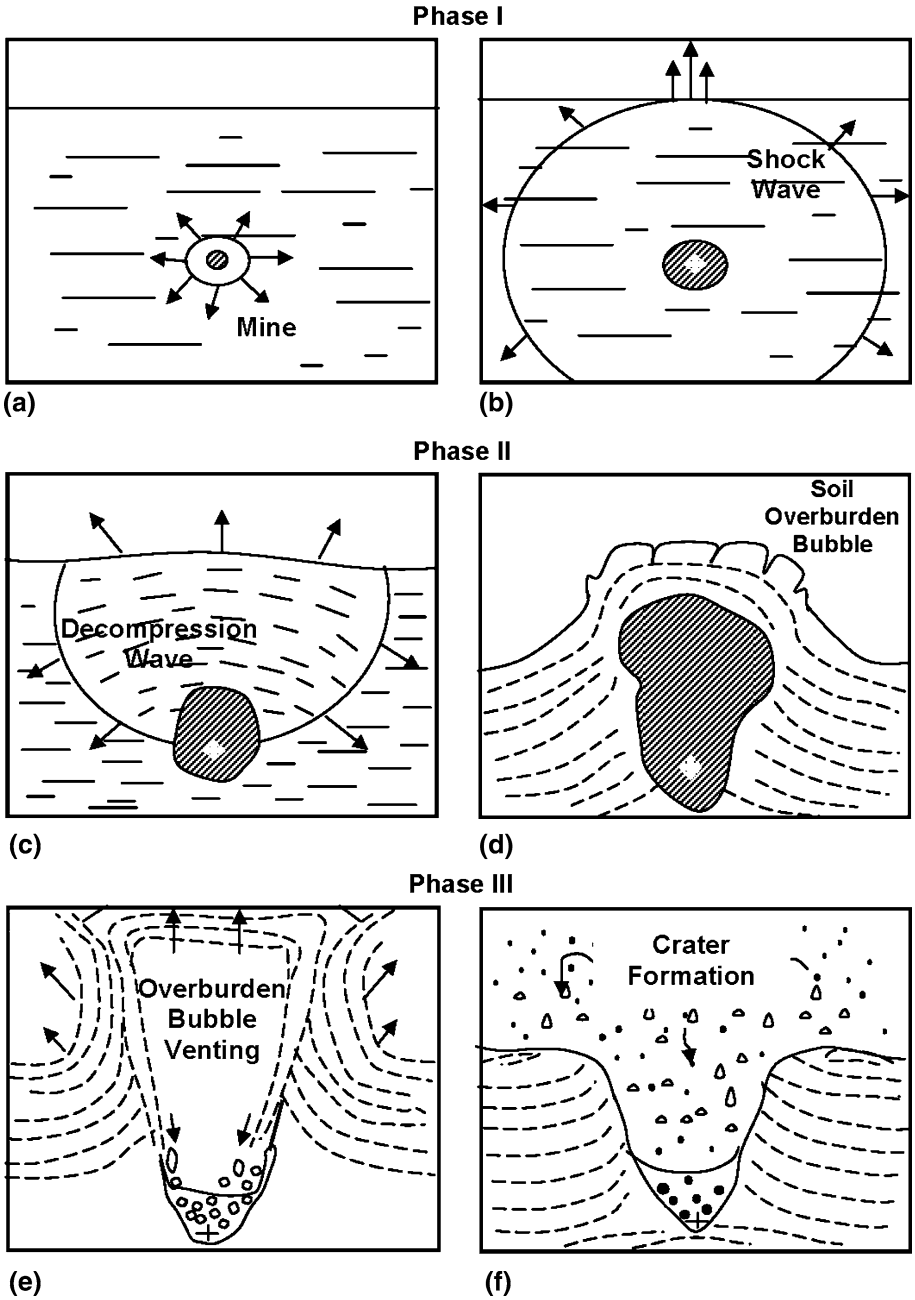

Fig. 1 Various phases of denotation of a landmine shallow buried in soil. Please see text for details

reversible/elastic deformation of the soil. Detonation of shallow-buried explosives is associated with the formation of three types of shock waves: a compressive, a shear, and a Rayleigh shock wave. The first two shock waves are spherical and their amplitude decays as an inverse of the square of the radial distance. On the other hand, the Rayleigh wave expands on a cylindrical front and its amplitude decays as inverse of the square-root of the radial distance. In general, the rate of decay of shock amplitude with radial distance is a strong function of the soil properties (e.g., microstructure, composition, level of hydration, etc.). It is generally believed that the first phase of shallow-buried mine detonation controls the amount of energy available for conversion into soil kinetic energy and it is well established (Ref 6, 10) that it is affected by the parameters such as mine shape, mine DOB, soil properties, etc.;

(b) Soil-overburden bubble initiation phase begins when the soil-borne compressible shock wave reaches the soil/air interface. At this point, due to a large soil/air shock-impedance mismatch, the transmitted compressive shock to air is relatively weak while the reflected (tensile) shock is quite strong. A combined action of the tensile shock and the expanding high-pressure detonation products causes the soil overburden to begin to expand outward in a (initially) hemi-spherical manner. This process, which takes place over a period of few milliseconds, eventually results in the rupture of soil overburden and venting of the detonation products; and

(c) Soil-ejecta formation phase within which swirling detonation products still residing with the cavity formed by the exploded mine interact with the soil surrounding the cavity. This process results in the ejection of high-velocity soil and in the creation of large craters. The ejecta trajectory (which is generally in the upward direction) falls within an inverted cone with an included angle (between 60 and 90°), which increases with decrease in DOB and soil compaction/density.

3. Discrete-Particle Soil Model (Ref 26)

In this section, a brief overview is provided of the discrete-particle soil model recently proposed by Deshpande et al. (Ref 26). Within the model of Deshpande et al. (Ref 26), soil is treated as an aggregate of discrete particles and the mechanical representation of the material is governed by the forces associated with the contact between particles.

In general, two limiting regimes of soil can be identified depending on the soil density: (a) the low-density regime, in which the soil particles are widely spaced, particle contacts are of short duration and can be treated as collisions. The behavior of this soil in the regime is typically represented using discrete-particle soil models, such as the one developed by Deshpande et al. (Ref 26) and (b) the high-density regime in which particle contacts are of long duration, so that, they can be considered as semi-permanent. The behavior of soil in this regime is typically represented using continuum-type soil models, such as the CU-ARL soil model.

Deshpande et al. (Ref 26) attempted to develop a simple discrete-particle soil model and extend it so that the model can be used over the intermediate density ranges. The key steps involved in the formulation of the soil model proposed by Deshpande et al. (Ref 26) can be summarized as follows:

(a) First, the parameters characterizing the outcome of particle interactions (i.e., the coefficient of restitution, e, and two-particle collision time, t_c) are related to the particle's mass and (normal) contact properties (specifically the normal contact stiffness, K_n and the normal contact damping coefficient, C);

(b) Next, a simple two-dimensional model was developed for a soil subjected to a strain-rate field characterized by a shear and a normal strain rate. This was done for a given (typical) set of particle contact conditions (e.g., pre-contact distance, collision angle, etc.), by calculating the momentum transfer per collision associated with particle interactions, by combining this result with the one for the average number of particle collisions per unit time and with the average collision cross-sectional area. Finally, an expression is derived for the rate of change of the specific impulse and used to define the repulsive internal pressure, P and the associated shear stress, τ; and

(c) The model developed in (b) is generalized to a three-dimensional formulation by: (i) replacing the shear and normal strain rates with the von-Mises, $\dot{\varepsilon}_e$ and volumetric, $\dot{\varepsilon}_m$, strain rates, respectively; (ii) replacing the cosine and sine of the collision angle, ω, with the so-called Bagnold parameters, α and β, respectively; (iii) by replacing the in-plane normal and shear stress with three-dimensional mean, σ_m and deviatoric, σ_e stresses, respectively; and (iv) by calculating the two stress components to get the total stress $\sigma_{ij} = \sigma_{e,ij} + \sigma_m\delta_{ij}$, where δ_{ij} (i = 1,2,3; j = 1,2,3) is the Kroenecker delta. The final equation for stress obtained is as follows:

$$\sigma_{ij}^{D} = \begin{cases} f(e,\lambda)\lambda\zeta\rho D^2\dot{\varepsilon}_f\left(\frac{2}{3}\alpha\varepsilon'_{ij} - \delta_{ij}\beta\dot{\varepsilon}_e\right), & \text{if } \dot{\varepsilon}_f > 0 \\ 0 & \text{otherwise} \end{cases}, \qquad \text{(Eq 1)}$$

where $\lambda = D/d$ is a linear concentration of particles, D is the (mono-size) particle diameter, d is the inter-particle distance, $\zeta = \pi(1+e)/6$, ρ is the solid density, $\dot{\varepsilon}_f = \alpha\dot{\varepsilon}_e - \beta\dot{\varepsilon}_m$, and $\dot{\varepsilon'}_{ij} = \dot{\varepsilon}_{ij} - \frac{\dot{\varepsilon}_m\delta_{ij}}{3}$.

The function $f(e, \lambda)$ in Eq 1 was derived in such a way that it is consistent with the following observations: (i) the stress varies inversely with the square of the inter-particle distance and (ii) in the limit of "plastic" particle collisions ($e \to 0$), the resulting stress is strain-rate independent (or more precisely, weakly dependent). Based on the above observation the following simple functional form was proposed: $f(e,\lambda) = e\lambda$.

The stress relation for σ_{ij}^{D} as prescribed by Eq 1 is associated with particle dynamic interactions (i.e., particle micro-inertia). This type of particle interactions is prevalent up to a critical soil density (typically described by the relative soil density, $\bar{\rho}_{crit}$). At densities exceeding $\bar{\rho}_{crit}$, the soil is perceived as being in a consolidated state so that, the total stress is defined as the sum of the micro-inertia stress, σ_{ij}^{D}, and a consolidated

stress, σ_{ij}^{c}. The latter stress is defined by a continuum-type material model (such as the CU-ARL model, in the present work).

4. Cu-ARL Soil Continuum-Level Model (Ref 10-13)

Within the continuum-type soil models (such as the CU-ARL model), soil granularity is not considered explicitly. However, granular nature of the soil is accounted for implicitly through the appropriate selection/formulation of the material constitutive equations. For example, to account for compaction-induced soil consolidation, inelastic deformation of the soil is allowed to take place not only under deviatoric stress conditions, but also under sufficiently high pressures. A typical continuum-type material model consists of a set of equations which define the relationships between the flow variables (pressure, mass density, energy density, temperature, etc.). These relations typically involve: (a) an equation of state, (b) a strength equation, (c) a failure equation, and (d) an erosion equation for each constituent material. These equations arise from the fact that, in general, the total stress tensor can be decomposed into a sum of a hydrostatic stress (pressure) tensor (which causes a change in the volume/density of the material) and a deviatoric stress tensor (which is responsible for the shape change of the material). An equation of state then is used to define the corresponding functional relationship between pressure, density and internal energy (temperature), while a strength relation is used to define the appropriate equivalent plastic strain, equivalent plastic strain rate, and temperature dependences of the equivalent deviatoric stress. In addition, a materials model generally includes a failure criterion, i.e., an equation describing the (hydrostatic or deviatoric) stress and/or strain condition(s) which, when attained, causes the material to fracture and lose its ability to support normal and shear stresses. The erosion equation is generally intended for eliminating numerical solution difficulties arising from highly disordered Lagrangian cells. Nevertheless, the erosion equation is often used to provide additional material failure mechanism especially in materials with limited ductility.

The CU-ARL soil model (Ref 10-13) contains all four aforementioned equations. These equations are based on the so-called "porous-material/compaction" representation of the soil microstructure.

Within the "porous-material/compaction" representation, soil is considered to generally have a complex structure consisting of mineral solid particles which form a skeleton. The pores between the solid particles are filled with either: (a) a low-moisture air (this type of soil is generally referred to as "dry soil"); (b) water containing a small fraction of air ("saturated soil"); or (c) with comparable amounts of water and air ("unsaturated soil"). The relative volume fractions of the three constituent materials in the soil (the solid mineral particles, water, and air) are generally quantified by the porosity, α, and the degree of saturation (saturation ratio), β, which are, respectively, defined as: $\alpha = 1 - \bar{\rho} = V_p/V$ and $\beta = V_w/V_p$, where V_p is the volume of void (pores), V_w is the volume of water, and V is the total volume.

The four equations constituting the CU-ARL soil model are overviewed in the following four subsections. While only the dry-soil rendition of the CU-ARL soil model is used in the present work, the overview includes the role of moisture within the soil.

4.1 Equation of State

For the CU-ARL soil model, a porous-material/compaction equation of state is used which is a particular form of the Mie-Gruneisen equation of state:

$$P = P_H + \Gamma\rho(E - E_H) \qquad \text{(Eq 2)}$$

in which the second term on the right-hand side of the Eq 2 is omitted. In Eq 2, the following nomenclature is used: P is pressure (a sum of the pore pressure and effective stress in the soil skeleton), ρ is the (current) mass density, Γ is the Gruneisen gamma parameter, E is the internal energy density, and the subscript H is used to denote the reference shock-Hugoniot level of a given quantity.

The Hugoniot pressure, P_H, is defined using the following stationary-shock relationship (Ref 27):

$$P_H = \frac{\rho_0 C_0^2 \eta}{(1 - s\eta)^2}, \qquad \text{(Eq 3)}$$

where $\rho_0 = (1 - \alpha_0)\rho_{ref} + \alpha_0\beta_0\rho_w$ is the initial soil material mass density, where C_0 is the speed of sound [in the homogenized soil medium as measured using the standard flyer-plate experiment setup at room temperature (Ref 8)], $\eta = \left(1 - \frac{\rho_0 - \alpha_0\beta_0\rho_w}{\rho - \alpha_0\beta_0\rho_w}\right) = \left(1 - \frac{(1-\alpha_0)\rho_{ref}}{\rho - \alpha_0\beta_0\rho_w}\right)$ is the compressibility ratio, ρ_w is the density of water and the parameter s represents a rate of increase of the (average) material-particle (not to be confused with soil particle) velocity, U_p, with an increase in the shock velocity, U_s and is defined by the relation:

$$U_s = C_0 + sU_p \qquad \text{(Eq 4)}$$

In the CU-ARL soil model equation of state, the aforementioned relations for ρ_0 and η are substituted in Eq 4 to get:

$$P = P_H = \frac{((1 - \alpha_0)\rho_{ref} + \alpha_0\beta_0\rho_w)C_0^2\left(1 - \frac{(1-\alpha_0)\rho_{ref}}{\rho - \alpha_0\beta_0\rho_w}\right)}{\left(1 - s\left(1 - \frac{(1-\alpha_0)\rho_{ref}}{\rho - \alpha_0\beta_0\rho_w}\right)\right)^2}, \quad \rho \le \rho_{comp} \qquad \text{(Eq 5a)}$$

and

$$P = P_H = P(\rho_{comp}) + C_0^2(\rho - \rho_{comp}), \quad \rho > \rho_{comp} \qquad \text{(Eq 5b)}$$

where $\rho_{comp} = \left(\frac{1-\alpha_0}{1-\alpha_0+\alpha_0\beta_0}\right)\rho_{ref} + \left(\frac{\alpha_0\beta_0}{1-\alpha_0+\alpha_0\beta_0}\right)\rho_w$ [same as ρ used in the Deshpande et al. (Ref 26)] is the density of the soil at full compaction.

To account for the effect of saturation/hydration on the values of material parameters C_0 and s, the results obtained in Ref 8, 17 are fitted to a low-order polynomial in which the coefficients are set to depend on the initial level of porosity and the reference density. The results of this curve fitting procedure can be found in Ref 17, Fig. 8(a) and (b), where the C_0 versus β_0 and the s versus β_0 functional relations are also given. These relations in conjunction with Eq 5a and 5b define the dependence of pressure on ρ_{ref}, α_0, β_0, and ρ.

The P versus ρ relation just derived is valid only during loading and only when such loading gives rise to irreversible/plastic compaction of the porous material. It should be noted that the term loading implies an event within which the

pressure is increased (and, in the case of plastic loading, a decrease in material porosity takes place). Conversely, unloading is associated with a decrease in pressure. As shown in our previous work (Ref 1), during unloading/elastic-reloading, the P versus ρ relationship is defined as $\frac{dP}{d\rho} = C_0^2(\rho_{ref}, \alpha_0, \beta_0)$, where the $C_0(\rho_{ref}, \alpha_0, \beta_0)$ relation can be found in Ref 17, Fig. 8(a).

4.2 Strength Model

Within the dry-soil rendition of the CU-ARL soil model, material strength (a quantity which quantifies material's resistance to inelastic distortive deformation) is assumed to be pressure dependent, controlled by inter-particle friction and to be defined by the following relation:

$$\sigma_{y,dry} = \phi_{dry} P_{dry} \approx \begin{cases} 1.3732 P_{dry} & 0 < P_{dry} \le P_{MC} \\ 1.3732 P_{MC} & P_{dry} > P_{MC} \end{cases} \quad \text{(Eq 6)}$$

In the case of saturated soil, the CU-ARL soil model defines pressure-dependent material strength as:

$$\sigma_{y,sat} = \begin{cases} \phi_{sat} P_{sat} & 0 \le P_{sat} \le P_{MC} \\ \phi_{sat} P_{MC} & P_{sat} > P_{MC} \end{cases} \quad \text{(Eq 7)}$$

where the yield-stress-to-pressure proportionality coefficient, ϕ_{sat}, is defined as:

$$\phi_{sat} = \begin{cases} \left(0.1 + 1.2732 \frac{P_{sat}}{P_{MC}}\right) & 0 \le P_{sat} \le P_{MC} \\ 1.3732 & P_{sat} > P_{MC} \end{cases} \quad \text{(Eq 8)}$$

The term P_{MC} (=1.864×10^5 kPa) appearing in Eq 6-8 is the Mohr-Coulomb pressure (a pressure threshold beyond which the material strength is pressure insensitive). It should be noted that none of the Eq 6-8 include the effect of strain rate on the soil material strength. This was justified in our previous work (Ref 17), where it was shown that as long as the model is used at high-deformation rates (ca. $> 1.0 \times 10^2$/s), the strength and failure behavior of soil can be considered rate independent.

Within the CU-ARL soil strength model, the strength versus pressure relationship for unsaturated soil is defined using a linear combination of the strength/pressure proportionality coefficients in dry and the saturated soils as:

$$\sigma_{y,unsat} = \begin{cases} \phi_{unsat} P_{unsat} & 0 \le P_{unsat} \le P_{MC} \\ \phi_{unsat} P_{MC} & P_{unsat} > P_{MC} \end{cases} \quad \text{(Eq 9)}$$

where

$$\phi_{unsat} = (1 - \beta_o)\phi_{dry} + \beta_o \phi_{sat} \quad \text{(Eq 10)}$$

Defined in this way, Eq 9 and 10 can be also used for dry soil ($\beta_0 = 0.0$) and saturated soil ($\beta_0 = 1.0$).

In addition to specifying the strength versus pressure relationship, the compaction strength model entails the knowledge of the density-dependent shear modulus. Since water has no ability to support shear stresses, the shear modulus, G, of unsaturated soil is dominated by the shear modulus of the solid skeleton of the soil. However, the presence of water changes the density of the soil. Therefore, the original compaction shear modulus versus density relationship for dry soil was appropriately modified by: (a) correcting density with a $-\alpha_0\beta_0\rho_w$ term and (b) introducing a moisture level-dependent maximum shear modulus in order to obtain a (deformation-rate independent) shear modulus versus density relationship for soil at different saturation levels. This procedure yielded the following shear modulus versus density functional relationships:

$$G(\text{kPa}) = \begin{cases} 5.2175 \times 10^{-14}(\rho - \alpha_0\beta_0\rho_w)^6 \\ \quad \rho(\text{kg/m}^3) < (1 - \alpha_0\beta_0)\rho_{ref} + \alpha_0\beta_0\rho_w \\ (1 - \alpha_0\beta_0) G_{Bulk} \\ \quad \rho(\text{kg/m}^3) \ge (1 - \alpha_0\beta_0)\rho_{ref} + \alpha_0\beta_0\rho_w \end{cases} \quad \text{(Eq 11)}$$

where G_{Bulk} (=3.73470×10^7) denotes the shear modulus of fully compacted dry soil. Equation 11 correctly accounts for the fact that, at full compaction, the soil density is equal to $(1 - \alpha_0\beta_0)\rho_{ref} + \alpha_0\beta_0\rho_w$.

It should be noted that in the strength model developed in this section, the contribution of water to the material strength was neglected. This can be justified by recognizing the fact that viscosity of water is typically about 0.001 Pa s and that even at very high-deformation rates (1.0×10^5/s), the contribution of water to the shear strength of the soil is merely about 100 Pa.

4.3 Failure Model

It is well established that the presence of moisture in soil increases the soil's cohesive strength (Ref 28). Therefore, the magnitude of the (negative) failure pressure for soil is expected to increase with the degree of saturation (β). Also, the moisture content should be substantial ($\beta > 0.7$) before its effect on the cohesive strength of soil becomes significant (Ref 28). To account for these two observations, within the CU-ARL soil failure model (Ref 17), the following expression was proposed for the magnitude of the (negative) failure pressure in unsaturated soil; $P_{fail\ unsat}$:

$$P_{fail,unsat} = \beta_0^5 P_{fail,sat} \quad \text{(Eq 12)}$$

where $P_{fail,sat}$ (set equal to 70 kPa) is the failure pressure in saturated soil (Ref 28). The relationship given by Eq 12 correctly predicts that the cohesive strength of unsaturated soil with a degree of saturation of 0.7 is about 10-15% of that in the saturated soil.

4.4 Erosion Model

Erosion of a porous-material element is assumed, within the CU-ARL soil erosion model, to take place when geometrical (i.e., elastic plus plastic plus damage) instantaneous strain reaches a maximum allowable value. The investigation reported in Ref 27 established that the optimal value for the geometrical instantaneous strain is ~1.0.

5. Soil-Slug Impact on a Rigid, Fixed Flat Target

As mentioned earlier, the main objective of the present work is to establish the extent of differences in the computational analysis based predictions obtained using a conventional continuum-type soil model (the CU-ARL soil model in the present case) or a discrete particle-based soil model [the model proposed by Deshpande et al. (Ref 26)]. The first computational analysis carried out in order to establish these differences pertains to the case of a rectangular soil slug impacting (at a zero obliquity angle) a rigid, fixed flat target surface. To mimic the conditions encountered near the center of the target surface when impacted with a spray of soil, zero normal-lateral strain

and a zero all-shear strain conditions are assumed. Thus, the problem analyzed is essentially of a one-dimensional nature, Fig. 2.

A schematic of the expected temporal evolution of soil within the slug is depicted in Fig. 3(a)-(d). In its initial state, Fig. 3(a), soil is treated as a loose aggregate of particles. After impact, the soil at the impacted end of the slug becomes compressed and a compressive shock wave begins to travel in the direction opposite to the slug-motion direction, Fig. 3(b). Soil particles swept by the compressive shock are brought to the state of rest while at the advancing shock front numerous particle collisions result in pronounced energy dissipation. When the (densifying) shock wave reaches the free end of the slug, it reflects as a tensile wave (or more precisely as a release wave). The tensile wave then travels toward the target surface and all the soil particles swept by this wave are imparted a velocity (i.e., a linear momentum) in the direction opposite to the initial motion direction of the slug, Fig. 3(c). When the release wave has managed to fully traverse the slug, all the particles are imparted this momentum and the slug, as a whole, separates from the target and continues to move in the direction opposite to the initial impact direction, Fig. 3(d). It is this (residual) momentum of the slug that governs the extent of momentum transfer to the target surface.

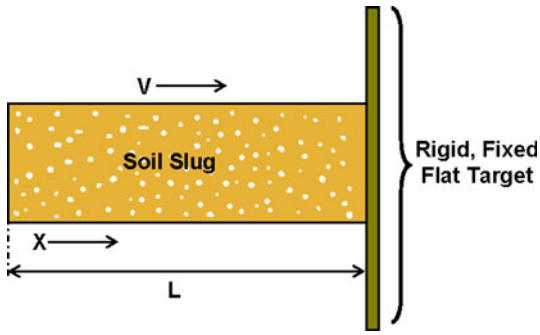

Fig. 2 A schematic for the problem involving impact of a rectangular soil slug impacting a rigid, fixed flat target

5.1 Problem Formulation

As mentioned above, the basic problem analyzed in this section is the one-dimensional impact of a soil slug against a rigid, fixed flat target surface. The case of a 0.03-m long rectangular soil slug was considered in the present work (slug lateral dimensions are irrelevant due to the one-dimensional nature of the problem at hand). The initial compaction state of the soil is defined by its initial density $\rho_{init} = \bar{\rho}_{init}\rho$, where $\bar{\rho}_{init}$ is the initial relative density (0.1 and 0.6 cases analyzed in the present work) and ρ is the solid density (=2700 kg/m^3). Only the case of dry soil (i.e., saturation-level equals zero) is analyzed. This is all that is needed to fully define the material initial state within the CU-ARL soil model. For the discrete-particle soil model of Deshpande et al. (Ref 26), the following additional soil parameters are used: particle diameter, D = 200 μm; critical relative volume fraction at the onset of soil consolidation, $\bar{\rho}_{crit} = 0.65$; particle-particle coefficient of restitution, e = 0.01 (elastic collision case) and e = 0.9 (plastic collision case); and Bagnold parameters, $\alpha = 0.1$ and $\beta = 0.3$.

5.2 Computational Procedure

The physical problem at hand is cast as a finite element problem and solved within a Lagrangian framework using ABAQUS/Explicit (Ref 29). Typically, 1000 eight-node first-order reduced-integration brick-type elements are used. The lateral nodal degrees of freedom are suppressed while all the slug nodes are initially assigned a constant velocity. Target is modeled as a rigid, fixed, flat analytical surface. Slug/target contact is modeled using a penalty contact algorithm. Within the penalty contact method, the penetration of the surfaces into

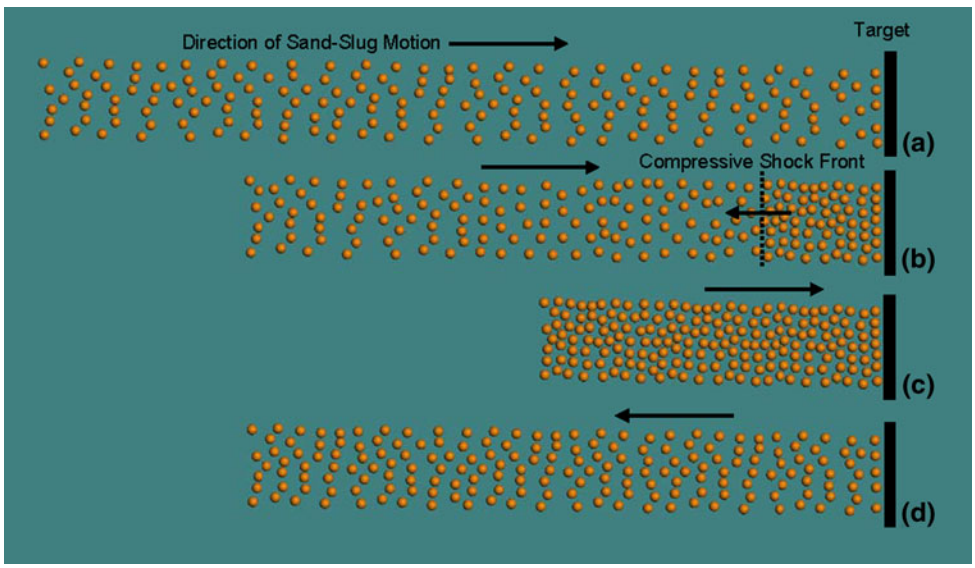

Fig. 3 Temporal evolution of the material within a laterally confined soil slug impacting a rigid, fixed flat target: (a) just prior to impact, (b) shortly after impact showing the partially densified soil slug with the densification front moving in the opposite direction to the slug initial motion direction, (c) the compressive densification front reflects from the back face of the slug resulting in the formation of tensile (release wave), and (d) the moment of arrival of the release wave to the slug/target interface leading to slug-target separation and a subsequent continuous motion of the slug in a direction opposite to its initial motion direction

each other is resisted by linear spring forces/contact pressures with values proportional to the depth of penetration. These forces, hence, tend to pull the surfaces into an equilibrium position with no penetration. Contact pressures between two bodies are not transmitted unless the nodes on the "slave surface" contact the "master surface." There is no limit to the magnitude of the contact pressure that could be transmitted when the surfaces are in contact. Transmission of shear stresses across the contact interfaces is defined in terms of a static and a kinetic/sliding friction coefficient and an upper-bound shear stress limit (a maximum value of shear stress which can be transmitted before the contacting surfaces begin to slide).

To accurately capture the shock/release wave-front structure, no artificial damping (a procedure which improves computational robustness) was used. As mentioned earlier, energy dissipation takes place at the wave front which, per se, helps stabilize the computational procedure.

Both the CU-ARL continuum-type soil model and the discrete particle-based soil model proposed by Deshpande et al. (Ref 26) are implemented as a VUMAT User-material subroutine and linked with the ABAQUS/Explicit (Ref 29) solver. It should be noted that although the soil model proposed by Deshpande et al. (Ref 26) is based on the treatment of soil as an aggregate of discrete particles, the final equation for the stress, Eq 1, is of a continuum type.

5.3 Results and Discussion

As mentioned earlier, the main objective of the present work was to identify the extent of changes in the computational results, which may occur, when one chooses the particle-based soil model proposed by Deshpande et al. (Ref 26) or the CU-ARL soil model (Ref 10-13) in the same transient nonlinear dynamics analysis. In principle, these differences are expected to depend on the initial state of soil and soil type. The initial state of the soil will be exemplified here by a single-material property, the initial density $\rho_{init} = \bar{\rho}_{init}\rho$. As far as the type of soil is concerned, it will also be represented by a single quantity, the particle-to-particle coefficient of restitution, e. This quantity depends on soil microstructure, composition (e.g., the percentage of clay, silt, gravel, etc.), the level of hydration, etc. In the case of dry sand-rich soil, e is expected to take a large (e.g., $e = 0.9$) value, representative of elastic type particle-particle collisions. On the other hand, in the case of clayey saturated soil, a low value of e (e.g., $e = 0.01$), representative of nearly perfectly plastic inter-particle collisions, is expected.

Based on the above considerations, four soil conditions/types are considered, each associated with the relative density $\bar{\rho}_{init} = 0.1$ (loose soil) or $\bar{\rho}_{init} = 0.6$ (partially consolidated soil) and one of the two values of the coefficient of restitution, $e = 0.9$ (dry clay-free sand) and $e = 0.01$ (clayey saturated soil).

Examples of the results obtained in this portion of the work are shown in Fig. 4-7. These results are analyzed in the remainder of this section.

Temporal evolution of the contact pressure at the slug/target interface at two levels of slug initial velocity (500 and 1000 m/s) and for the four soil initial states/types is depicted in Fig. 4(a)-(d). Dashed and solid curves are used to denote the results based on the combined use of the particle-mechanics/consolidation soil model and on the use of consolidation soil model only, respectively. This curve-type designation is maintained throughout the remainder of the manuscript. Also, for Fig. 4-7, parts (a)-(d) correspond, respectively, to the following $\bar{\rho}_{init}/e$ combinations:

(a) 0.1/0.9, (b) 0.6/0.9, (c) 0.1/0.01, and (d) 0.6/0.01. Examination of the results displayed in Fig. 4(a)-(d) reveals that:

(a) the magnitude of the contact pressure increases while slug-target contact time decreases with an increase in the slug initial velocity;
(b) the extent of agreement between the corresponding results obtained using the two soil models is highly dependent on the soil initial density. That is, for the case of loose soil, Fig. 4(a) and (c), the corresponding results differ considerably while in the case of consolidated soil, Fig. 4(b) and (d), a relatively good agreement exists between the two sets of computational results;
(c) under the loose-soil conditions, Fig. 4(a) and (c), the CU-ARL soil model greatly over predicts the contact pressures and somewhat less under-predicts the contact time. Consequently, the specific momentum transferred to the target which is numerically equal to the area under the pressure versus post-impact time curve is significantly over predicted in the case of the CU-ARL soil model; and
(d) the effect of the particle-to-particle coefficient of restitution on the contact pressure and the contact time is of a secondary nature in the case of the combined soil model (and somewhat increases with the slug initial velocity and soil initial density) and is absent in the case of the CU-ARL soil model.

Spatial variation of the soil material-particle velocities (normalized by the slug initial velocity) at different post-impact times for the case of slug initial velocity of 1000 m/s for the four soil initial states/types is depicted in Fig. 5(a)-(d). It should be noted that (slug initial-length normalized) undeformed spatial coordinates are used as the abscissa in Fig. 5(a)-(d). Also, it should be noted that, since qualitatively similar results were obtained at other slug initial velocities, these additional results are not included here. Examination of the results displayed in Fig. 5(a)-(d) reveals that:

(a) As expected, impact of the slug against the rigid fixed target causes generation of a shock wave moving toward the free end of the slug (located at $x/L = 0.0$). The material swept by the shock wave has been brought into the zero velocity state. On the reflection of the shock wave from the slug free end, a release/tensile wave is generated and begins to move toward the target. In the slug region swept by the release wave, material particles are imparted a velocity opposite to the slug initial direction of motion;
(b) In the case of loose soil, Fig. 5(a) and (c), the two soil models yield considerably different results while in the case of the consolidated soil, Fig. 5(b) and (d), the agreement is reasonable;
(c) While the CU-ARL model predicts that (under all four conditions of soil microstructure/initial state) the slug bounces back at a velocity which is effectively of equal magnitude to the slug initial velocity, in the case of the combined particle-mechanics/CU-ARL soil model, the

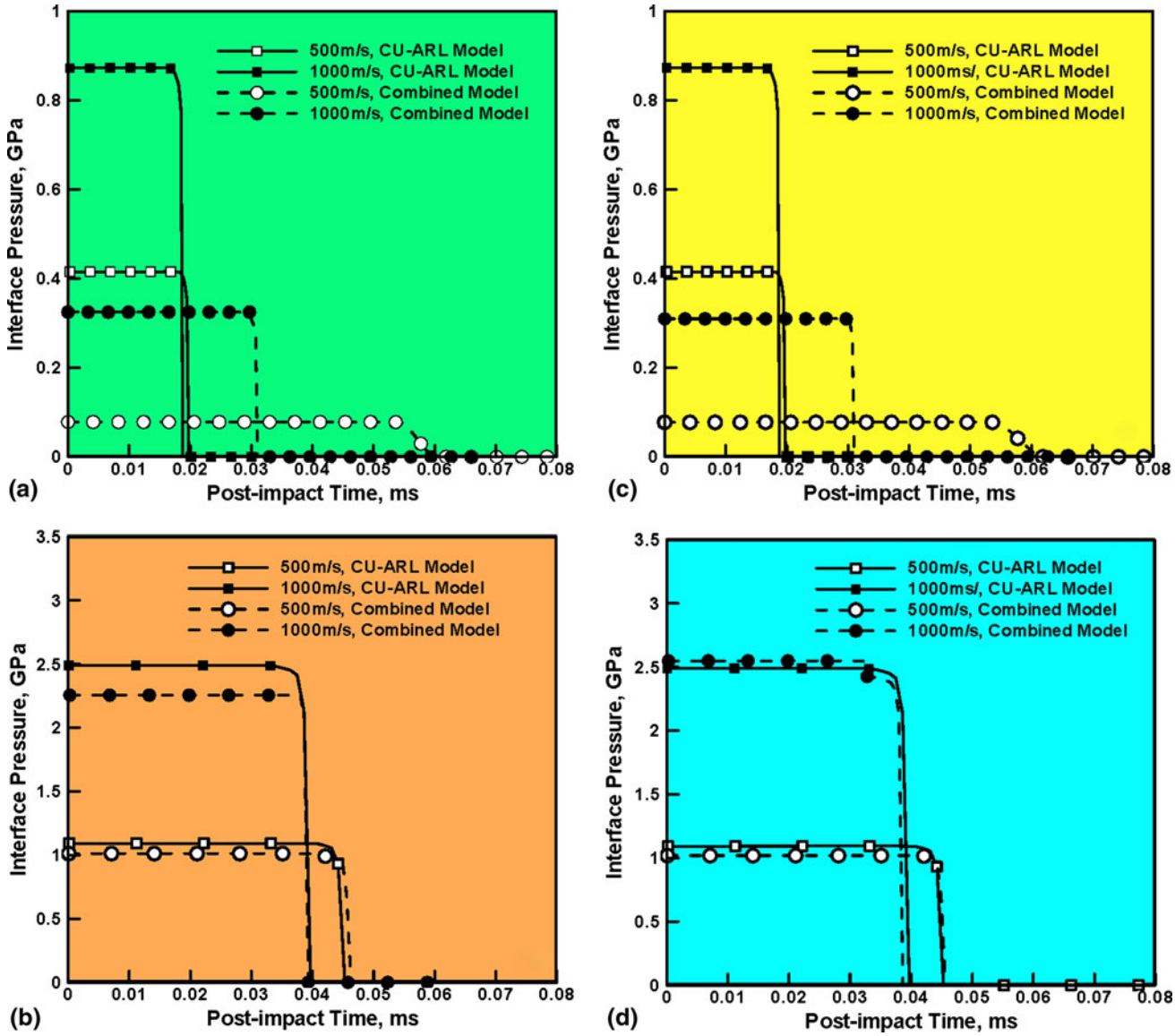

Fig. 4 Temporal evolution of the slug/target contact pressure at two slug velocities (500 and 1000 m/s) for the relative initial density $\bar{\rho}_{init}$ and the coefficient of restitution, *e*, equal to (a) 0.1/0.9, (b) 0.6/0.9, (c) 0.1/0.01, and (d) 0.6/0.01

slug residual velocity is lowered (i.e., the momentum transferred to the target is also lowered), by a particle-to-particle coefficient of restitution dependent amount; and

(d) The sharpness (i.e., the extent of dispersion) of the shock wave/release wave front is controlled by the magnitude of the particle-to-particle coefficient of restitution in the case of the combined soil model. Specifically, at small values of *e*, Fig. 5(c) and (d), the wave front is sharp, while at large values of *e*, Fig. 5(a) and (b), the wave front is spread out. Since the CU-ARL model does not include explicitly the particle-to-particle coefficient of restitution, the results displayed in Fig. 5(a)-(d) based on the CU-ARL model are not affected by the *e*-value.

Spatial variation of the soil relative density at different post-impact times for the case of slug initial velocity of 1000 m/s for the four soil initial states/types is depicted in Fig. 6(a)-(d). Examination of the results displayed in Fig. 6(a)-(d) reveals that these results are the expected counterparts of the results displayed in Fig. 5(a)-(d). Namely, shock loading of the slug densifies the soil within the slug, while the passage of a subsequent release wave (not shown for brevity) reduces the density. These findings are in agreement with the basic theory of shock-wave generation and propagation which states that at the shock front the material changes between the pre-shock and the post-shock states along the so-called Rayleigh line (a line along which material state variables, such as the particle velocity and the mass density, are related via a simple functional relation).

Variation of the momentum (more precisely impulse) transferred to the target, normalized by the slug initial momentum, with changes in the slug initial velocity for the four soil initial states/types is depicted in Fig. 7(a)-(d). Examination of the results displayed in Fig. 7(a)-(d) reveals that:

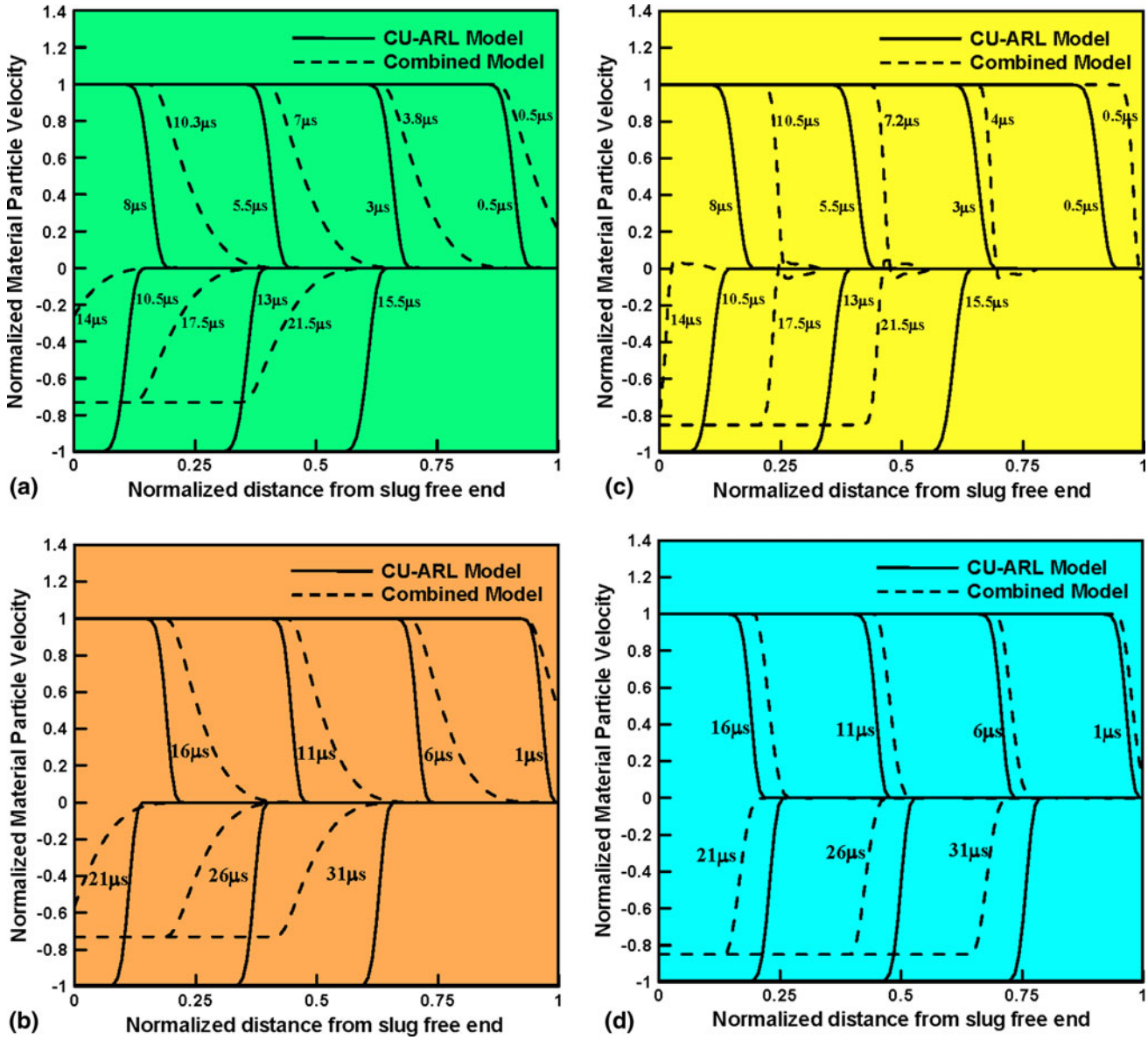

Fig. 5 Spatial distribution of the (slug initial velocity) normalized slug-particle velocities at different slug/target post-impact times for the case of 1000 m/s slug initial velocity and for the relative initial density, $\bar{\rho}_{init}$, and the coefficient of restitution, e, equal to: (a) 0.1/0.9, (b) 0.6/0.9, (c) 0.1/0.01, and (d) 0.6/0.01

(a) When the soil is initially in a consolidated state, Fig. 7(b) and (d), the transferred-momentum ratios predicted by the two soil models are quite comparable over a relatively large range of slug initial velocity. In sharp contrast, in the case of the loose soil, Fig. 7(a) and (c), the CU-ARL soil model tends to substantially over predict the transferred-momentum ratio over the entire slug initial velocity range; and

(b) The effect of particle-to-particle coefficient of restitution is of a secondary nature suggesting that most of the kinetic energy carried by the soil particles is dissipated at the advancing shock front. It should be noted that this finding is in sharp contradiction with the case of a single soil particle impacting the target with the particle/target collision being characterized by the coefficient of restitution, e. In the latter case, the corresponding normalized transferred momentum is equal to $1 + e$ and the extent of energy dissipation is greatly affected by the magnitude of e.

6. Detonation of a Soil-Buried Mine

The second case analyzed in the present work involves detonation of a circular disc-shaped mine buried in soil at a certain depth and the interactions between gaseous detonation products, mine fragments, and soil ejecta with a square-plate target located at some stand-off distance from the soil/air interface.

The interactions between gaseous detonation products, mine fragments, and soil ejecta with the target typically take place in close proximity of the mine detonation. Consequently, details regarding the charge size/shape, local soil properties, depth of

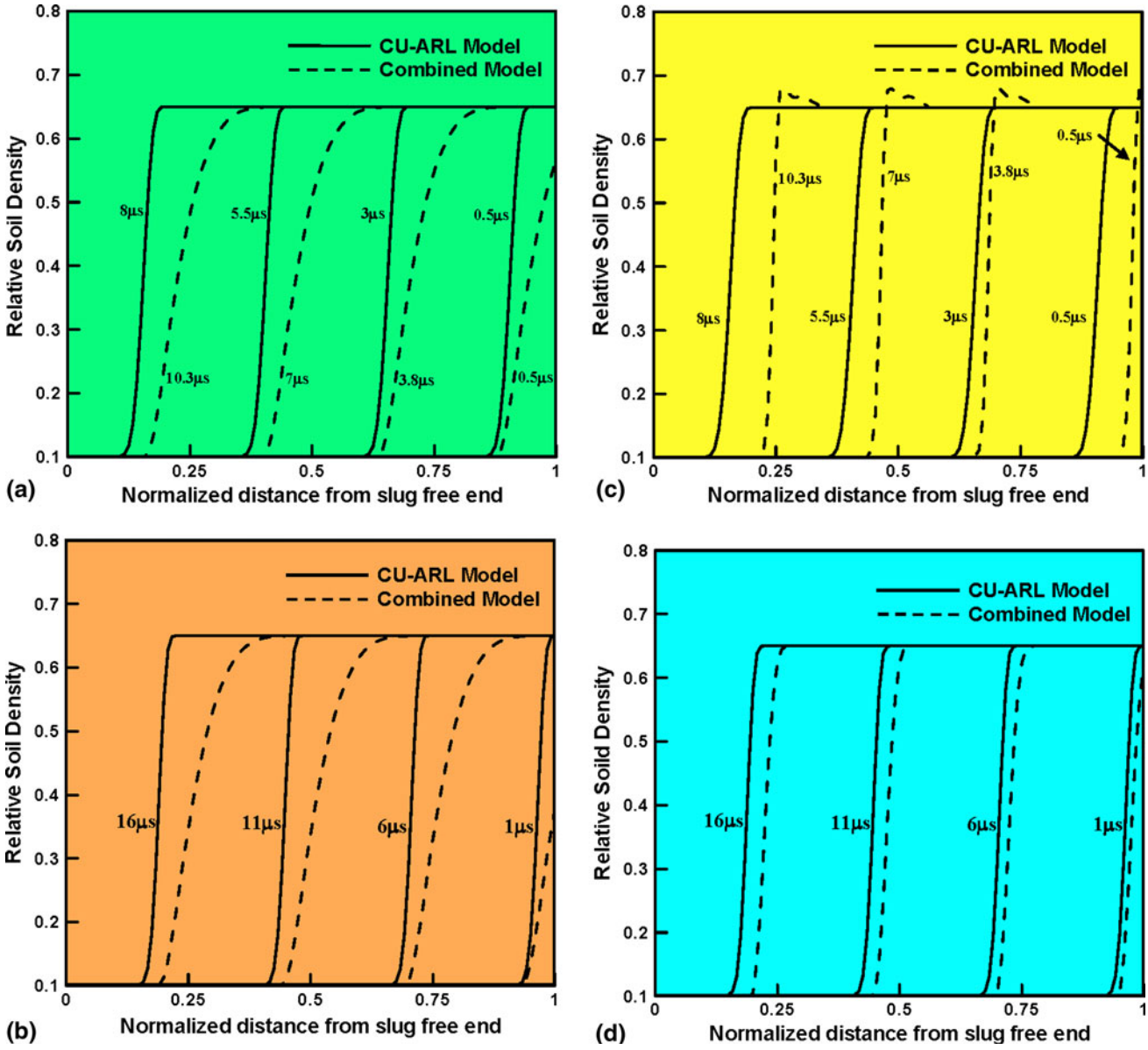

Fig. 6 Spatial distribution of the slug-relative density at different slug/target post-impact times for the case of 1000 m/s slug initial velocity and for the relative initial density $\bar{\rho}_{init}$, and the coefficient of restitution, e, equal to: (a) 0.1/0.9, (b) 0.6/0.9, (c) 0.1/0.01, and (d) 0.6/0.01

burial, target stand-off distance, etc. greatly influence these interactions. It should be noted, however, that except when the target is ground laid, the shock wave from the detonation does not make a significant direct contribution to the target blast loading, although, as will be discussed below it may play an important indirect role in the initial stages of target loading (through modifications in the soil-overburden shape and properties). It is well established that the primary target loading mechanism due to a buried-mine detonation is associated with the soil being driven into the target by the expanding gaseous detonation products (e.g., 30, 31).

Target loading is typically divided into two well-defined temporal phases:

(a) an initial short-duration loading phase within which the soil-cap/overburden impacts only a relatively small section of the target surface. Nevertheless, due to attendant high-impact/stagnation pressures, about half of the total momentum is transferred to the target during this loading phase. Due to close proximity of the target, geometrical and material properties of the soil cap play a critical role in this phase of target loading. It is recognized that while shock waves (either soil-borne or air-borne) do not directly affect the momentum transfer, they can play an important role in modifying the properties and configuration of the soil overburden from its pre-blast state to its state at the moment of collision with the target. This role of the shock waves is related to the fact that, due to a high soil/air shock-impedance mismatch, the arrival of these waves to the soil/air interface results in the formation of strong soil-borne release waves and very weak air-borne shock waves. As a result of the back-propagating release waves, soil overburden is transformed into a low-density expanding dome. It is the impact of the soil within this dome that controls the temporal evolution and spatial distribution of the

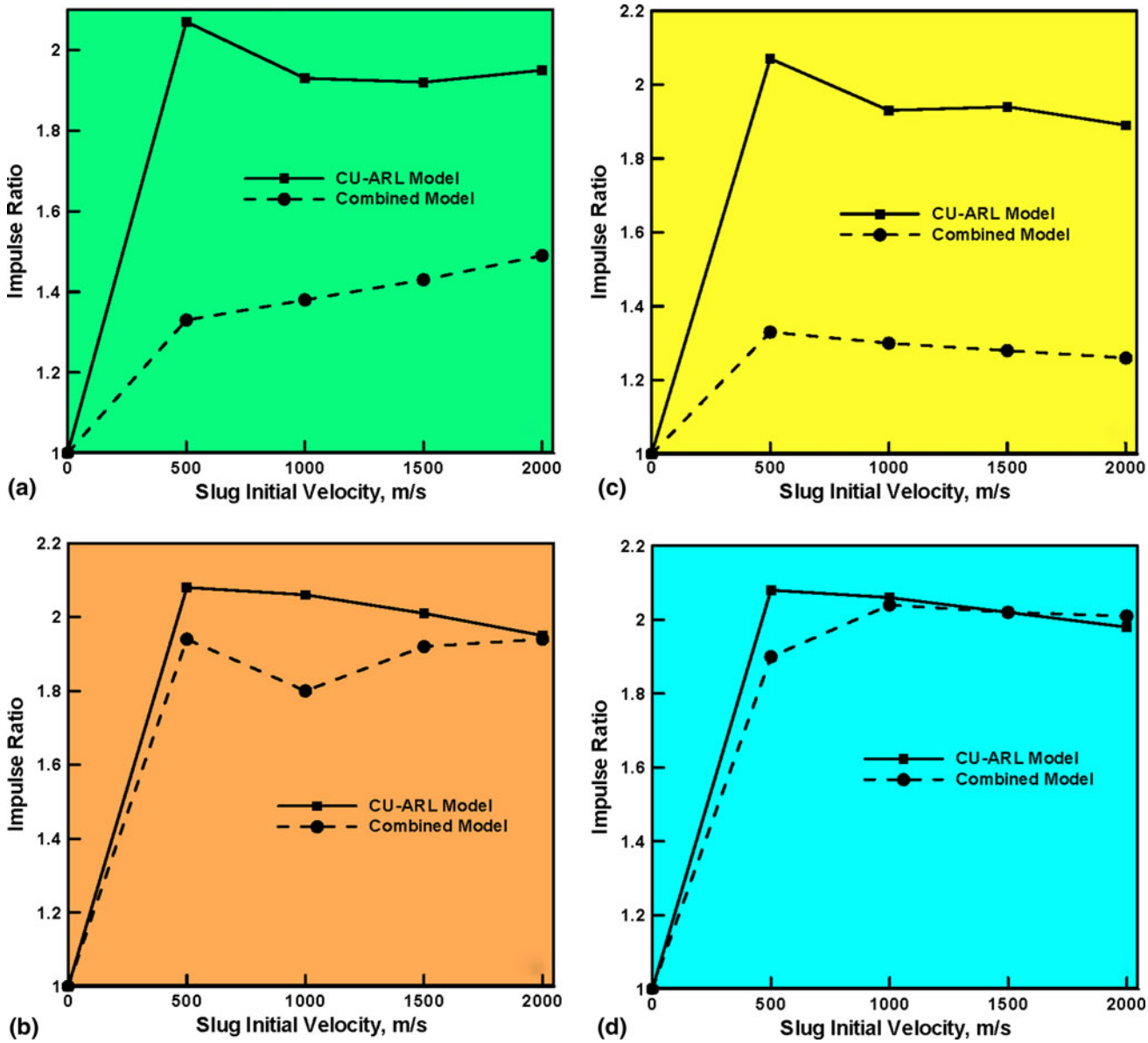

Fig. 7 The effect of slug initial velocity on the ratio of transferred momentum to the initial slug momentum for the relative initial density, $\tilde{\rho}_{init}$, and the coefficient of restitution, e, equal to: (a) 0.1/0.9, (b) 0.6/0.9, (c) 0.1/0.01, and (d) 0.6/0.01

stagnation pressure over the target impact surface; and

(b) a subsequent (at least an order of magnitude) longer-duration loading phase within which extensive excavation of the soil outside the radius of the soil cap and crater formation take place. The scooped out soil travels upward essentially parallel to the instantaneous wall of the crater being excavated and forms an annulus of soil hitting the target. In sharp contrast to the initial loading phase in which the velocity of the soil cap is dominated by its component normal to the target surface, comparable normal and tangential soil-velocity components are observed in this phase. As the soil excavation proceeds, the radius and the thickness of the soil annulus continue to increase (the former, at a decreasing, while the latter, at an increasing rate).

An additional effect arises when the soil annulus stagnating on the target plate confines the gaseous detonation products between the crater and the bottom of the target plate. This may allow the gaseous detonation products to exert additional (although minor) loading on the target plate (as long as the associated gage pressure is positive). The analysis presented above suggests that the stagnation pressures in this loading phase are substantially lower than in the initial loading phase. Nevertheless, the momentum transferred is comparable to the one associated with the initial loading phase due to longer loading times and a larger section of the target surface being impacted by soil/detonation products.

From the practical point of view, both the temporal evolution and spatial distribution of the stagnation pressure over the target surface and the total impulse transferred to the target are of interest. Excessive local pressures can lead to structural failure (including excessive deflections, fracture, buckling, etc.) while excessive total momentum can result in prohibitively large structural motion. Consequently, the main objective of this portion of the work was to establish the extent

of differences in the stagnation peak pressure and in the total momentum transfer resulting from a different selection of the soil material model in the computational analyses.

6.1 Problem Formulation

Since one of the main requirements of a computational analysis like the one presented here is to correctly predict the peak stresses, their spatial distribution and the total impulse transferred to a target, a simple square target plate is placed at a stand-off distance from the soil/air interface. A schematic of the geometrical model and the physical problem at hand is presented in Fig. 8. It should be noted that due to the presence of two orthogonal planes of symmetry, only one quarter of the geometrical domain had to be modeled. A number of cases differing relative to the explosive charge type, size (the diameter-to-height ratio = 3.0 was kept constant) and the depth of burial of the mine, and target edge-length and stand-off distance are analyzed. Since variations in these parameters did not affect qualitatively the overall findings yielded by the present analysis, only the results pertaining to one of these cases is presented here. The case presented here involved a C4 HE (density = 1601 kg/m^3) mine with a diameter D = 242.7 mm, depth of burial = 152.4 mm (relative to the top face of the mine), target edge-length = 500 mm and target stand-off distance = 152.4 mm.

The geometrical model displayed in Fig. 8 is next preprocessed (meshed) using the general purpose preprocessing program HyperMesh from Altair Inc. (Ref 32). The (quarter solid-cylinder minus a quarter circular-disc mine region) soil computational domain was typically assigned a radius of 400 mm and a height of 500 mm. The domain was divided into three concentric subdomains. All three subdomains were meshed using eight-node reduced-integration continuum elements with a typical edge length of 5, 10, and 20 mm (starting from the innermost zone), respectively. The lateral and the bottom faces of the soil domain were subsequently surrounded with eight-node infinite elements in order to model far-field soil regions and avoid un-physical stress-wave reflection at the soil-domain lateral and bottom surfaces. The soil domains containing noninfinite elements were filled with either the particle-based soil model by Deshpande et al. (Ref 26) or with CU-ARL soil model (Ref 10-13), while the infinite elements were filled with an "elastic" soil material with a Young's modulus and a Poisson's ratio matching those of the soil models used to fill the interior portion of the soil domain. The size and circular-disk shape of the mine computational domain are selected to match the corresponding hole within the soil and meshed using eight-node first-order reduced-integration continuum elements with a typical edge length of 5 mm. The mine domain is filled with C4 HE material, whose behavior was characterized by the Jones-Wilkins-Lee model (Ref 33). The previously mentioned "penalty contact" algorithm was used to model interaction between the gaseous detonation products of the mine and the surrounding soil (as well as between detonation products, soil, and the target).

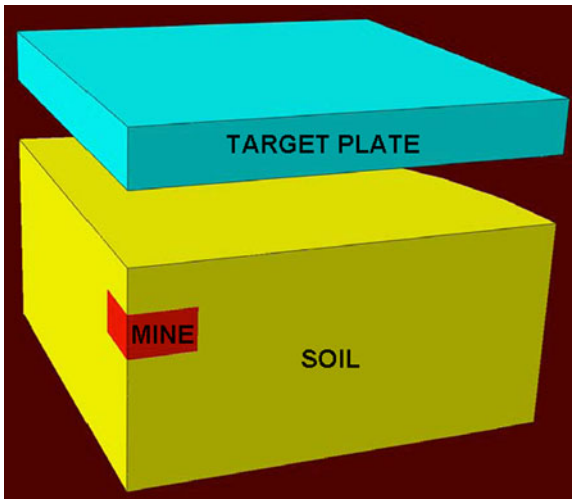

Fig. 8 A schematic of the geometrical domains used in the computational analysis of detonation of a C4 mine buried in soil

The target plate domain was meshed using eight-node first-order reduced-integration continuum elements with a typical edge length of 5 mm and filled with AISI 4340 steel. The dynamic behavior of this steel was modeled using a linear equation of state and a Johnson-Cook strength and failure models. Details regarding the material model for AISI 4340 steel can be found in Ref 34.

6.2 Computational Procedure

The present nonlinear dynamics computational analysis of buried-mine detonation and the interaction of detonation products, soil ejecta with the target plate involved the following steps: (a) at the beginning of the simulation, the target plate, the mine, and the soil are all assumed to be at rest (with the gravitational force acting downward); (b) mine detonation is next initiated either over the entire bottom face of the mine or at the bottom center; and (c) the mechanical response of the target plate to impact by the soil ejecta and the detonation products is monitored in order to determine the spatial distribution and temporal evolution of pressure and specific impulse over the surface of the target. To ensure fidelity of this approach, i.e., in order to ensure that the results obtained are insensitive to the size of the elements used, a standard mesh-sensitivity analysis had to be carried out (the results not shown for brevity).

6.3 Results and Discussion

As in the case of the slug-impact case analyzed in the previous section, here the attention is focused on the four cases of soil initial state/constitution. As discussed earlier, in the case of targets being subjected to detonation mine loads, both the peak pressure experienced and the total momentum transferred to the target are of concern. That is the reason both quantities are analyzed here as a function of the soil material model used and as a function of the soil initial state/configuration.

Examples of the typical results obtained in this portion of the work which pertain to the spatial distribution of the mass density within the soil in the initial short-duration loading phase and in the subsequent long-duration loading phase are presented in Fig. 9(a)-(b), respectively. In Fig. 9(a), the effect of release wave (generated at the soil/air interface) in reducing density in the soil cap is evident. On the other hand, the effect of shock-wave-induced consolidation of the soil surrounding the detonation gas bubble is clearly visible in Fig. 9(b).

Variation of peak stagnation pressure as a function of radial distance from the target-plate center for the four cases of the soil initial state/configuration are depicted, respectively, in Fig. 10(a)-(d). Again, the results associated with the continued use of the particle-based model proposed by Deshpande et al.

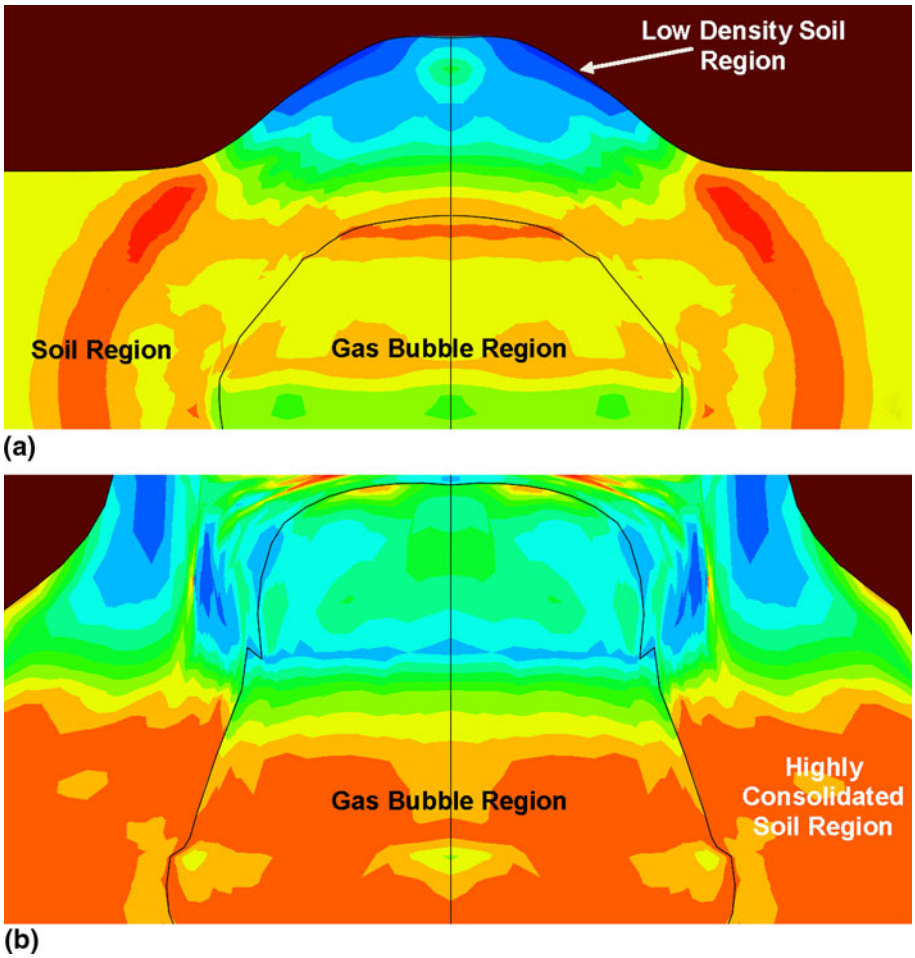

Fig. 9 Typical results pertaining to the spatial distribution of density within soil in: (a) the initial short-duration loading phase and (b) the subsequent long-duration loading phase

(Ref 26) and the CU-ARL soil model (Ref 10-13) are denoted using dashed curve representation, while the results obtained using CU-ARL soil model only are depicted using solid curves. Examination of the results displayed in Fig. 10(a)-(d) reveals that:

(a) In the case of soil which was initially consolidated, Fig. 10(b) and (d), the choice of the soil material model is not very critical. On the other hand, 15-20% higher pressures are obtained when the CU-ARL soil model is used to represent dynamic behavior of the loose soil, Fig. 10(a) and (c);
(b) The effect of the particle-to-particle coefficient of restitution is significant in the case of loose soil, Fig. 10(a) and (c) and is of a secondary nature in the consolidated soil case, Fig. 10(b) and (d); and
(c) As expected, the stagnation pressure is the highest at a zero radial distance and tapers off with radial distance.

The effect of the soil initial microstructure and constitution and of the choice of the soil material model on the total momentum transferred to the target plate for the four $\bar{\rho}_{\text{init}}/e$ combinations analyzed is summarized in Table 1. Examination of this table shows that the results are fully consistent with the corresponding stagnation peak pressure results displayed in Fig. 10(a)-(d). Namely:

(a) In the case of soil which was initially consolidated, the soil models predict comparable levels of the total impulse transferred to the target. In sharp contrast, in the case of the loose soil, the CU-ARL model substantially over predicts that total impulse transferred; and
(b) The magnitude of the particle-to-particle coefficient of restitution affects the total impulse transferred at low soil initial densities and does have a significant effect in the consolidated-soil case.

7. Summary and Conclusions

Based on the results obtained in the present work, the following main summary remarks and conclusions can be drawn:

1. The effect of the choice of soil model on the key computational results obtained in two transient nonlinear dynamics computational analyses is investigated. The first analysis deals with the normal impact of a rectangular soil slug on to a fixed rigid target while the second analysis deals with detonation of a shallow-buried mine and the subsequent interactions of the detonation products and soil ejecta with an AISI 4340 steel target plate. Two

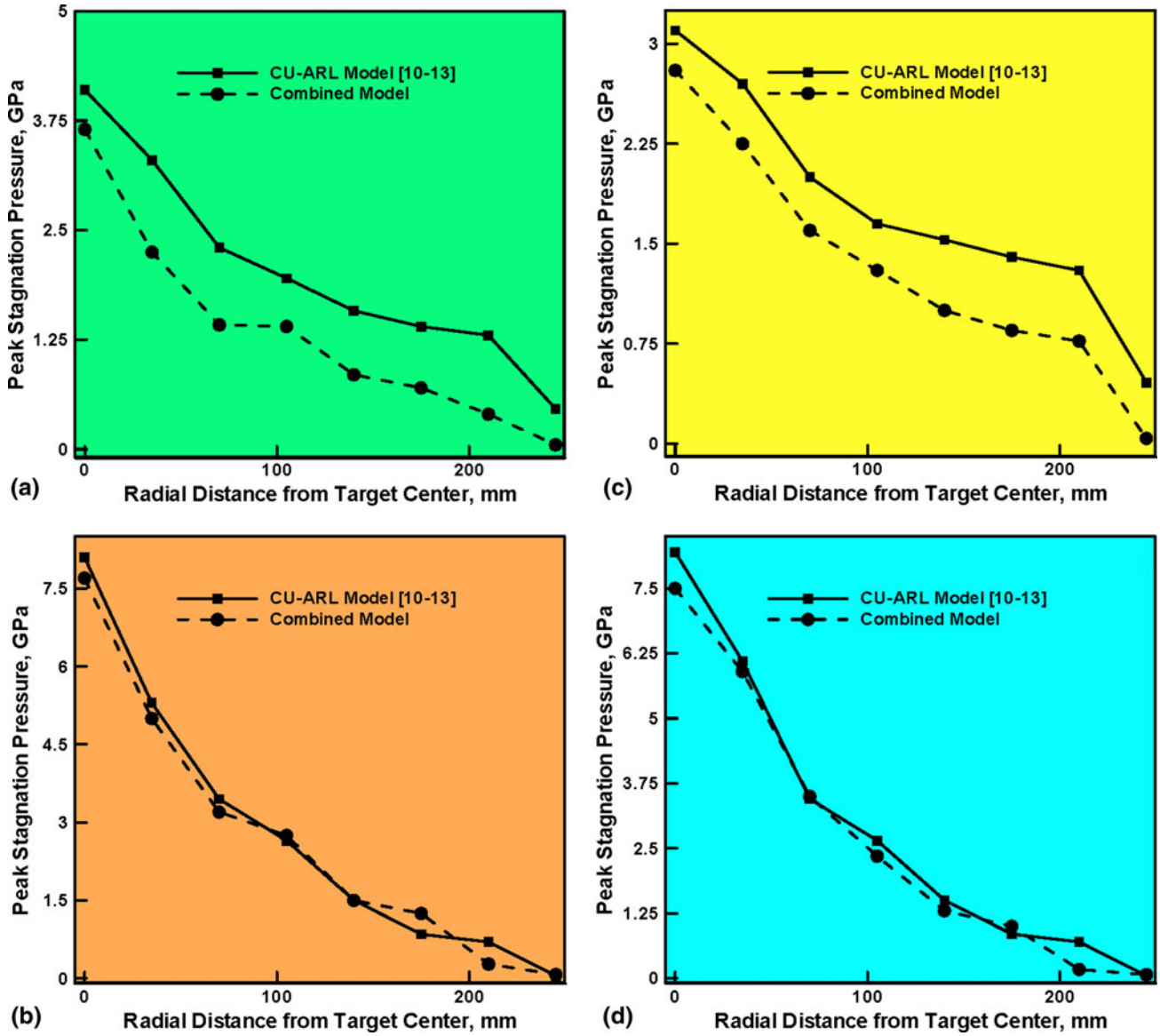

Fig. 10 Variation of the peak stagnation pressure with the radial distance from the target center for the relative initial density $\bar{\rho}_{init}$, and the coefficient of restitution, *e*, equal to: (a) 0.1/0.9, (b) 0.6/0.9, (c) 0.1/0.01, and (d) 0.6/0.01

Table 1 The effect of the choice of the soil model (i.e., a combined use of the particle-based (Ref 26) and the CU-ARL (Ref 10-13) models vs. the CU-ARL model alone) on the total impulse transferred to a 500 mm by 500 mm by 25.4 mm AISI 4340 steel target plate for 6.0 kg mass, 242.7 mm diameter, diameter-to-height ratio = 3.0, C4 mine, 152.4 mm depth of burial and 152.4 mm target stand-off distance and for the four cases of soil initial state/constitution

	Coefficient of restitution, *e*	
	0.01	**0.9**
Initial relative density $\bar{\rho}_{init}$		
0.1	$9.49 \times 10^3/1.42 \times 10^4$[a]	$1.24 \times 10^4/1.70 \times 10^4$
0.6	$2.48 \times 10^4/2.54 \times 10^4$	$2.52 \times 10^4/2.55 \times 10^4$

[a]Combined soil model-based result/CU-ARL model-based result

soil models are considered: one based on the combined use of a particle-mechanics and a consolidated-continuum soil representations and the other which considers soil as a continuum material only.

2. To rationalize the results in terms of the soil initial microstructure and constitution, the effect of two material coefficients, i.e., the soil initial relative density and the particle-to-particle coefficient of restitution is analyzed. The initial relative density was used to differentiate between loose and compacted soil while the particle-to-particle coefficient of restitution was used to differentiate between the behavior of a dry sandy and saturated-clayey soil.
3. The results obtained suggest that, in general, the use of the computationally demanding particle mechanics-based soil model is justified only in the low initial-density soil cases and that the magnitude of the particle-to-particle coefficient of restitution has a measurable effect only in

the case of the loose soil. This finding suggested that the effective coefficient of restitution for an agglomerate of soil particles may have a significantly different value than the individual particle coefficient of restitution.

References

1. M. Grujicic, B. Pandurangan, and B. Cheeseman, The Effect of Degree of Saturation of Sand on Detonation Phenomena Associated with Shallow-Buried and Ground-Laid Mines, *J. Shock Vib.*, 2006, **13**, p 41–62
2. D. Bergeron and J.E. Trembley, Canadian Research to Characterize Mine Blast Output, *16th International MABS Symposium*, Oxford, UK, September 2000
3. K.A. Holsapple and K.R. Housen, Crater Database and Scaling Tools, http://keith.aa.washinton.edu/craterdata, November 2004
4. P.S. Westine, B.L. Morris, P.A. Cox, and E. Polch, "Development of Computer Program for Floor Plate Response From Land Mine Explosions," Contract Report No. 1345, U.S. Army TACOM Research and Development Center, 1985
5. B.L. Morris, "Analysis of Improved Crew Survivability in Light Vehicles Subjected to Mine Blast," Final Report for Contract No. DAAK70-92-C-0058, U.S. Army Belvoir RDEC, Ft. Belvoir, VA, 1993
6. D. Bergeron, S. Hlady, and M.P. Braid, Pendulum Techniques to Measure Land Mine Blast Loading, *17th International MABS Symposium*, Las Vegas, June 2002
7. M.P. Braid, *Experimental Investigation and Analysis of the Effects of Anti-Personnel Landmine Blasts*, Defence R&D Canada, Suffield Special Publication, DRES SSSP 2001-188, December 2001
8. A.M. Bragov, A.K. Lomunov, I.V. Sergeichev, K. Tsembelis, and W.G. Proud, The Determination of Physicomechanical Properties of Soft Soils From Medium to High Strain Rates, *Int. J. Impact Eng.*, 2008, **35**(9), p 967–976
9. D.J. Chapman, K. Tsembelis, and W.G. Proud, The Behavior of Water Saturated Sand Under Shock-Loading, *Proceedings of the 2006 SEM Annual Conference and Exposition on Experimental and Applied Mechanics*, Vol 2, 2006, p 834–840
10. M. Grujicic, B. Pandurangan, J.D. Summers, B.A. Cheeseman, and W.N. Roy, Application of the Modified Compaction Material Model to Soil With Various Degrees of Water Saturation, *Shock Vibr.*, 2008, **15**, p 79–99
11. M. Grujicic, B. Pandurangan, N. Coutris, B.A. Cheeseman, W.N. Roy, and R.R. Skaggs, Derivation and Validation of a Material Model for Clayey Sand for Use in Landmine Detonation Computational Analysis, *Multidiscip. Model. Mater. Struct.*, 2009, **5**(4), p 311–344
12. M. Grujicic, B. Pandurangan, N. Coutris, B.A. Cheeseman, W.N. Roy, and R.R. Skaggs, Computer-Simulations Based Development of a High Strain-rate, Large-Deformation, High-Pressure Material Model for STANAG 4569 Sandy Gravel, *Soil Dyn. Earthq. Eng.*, 2008, **28**, p 1045–1062
13. M. Grujicic, B. Pandurangan, N. Coutris, B.A. Cheeseman, W.N. Roy, and R.R. Skaggs, Derivation, Parameterization and Validation of a Sandy-Clay Material Model for Use in Landmine Detonation Computational Analyses, *J. Mater. Eng. Perform.*, 2010, **10**(3), p 434
14. M. Grujicic, B. Pandurangan, and B.A. Cheeseman, A Computational Analysis of Detonation of Buried Mines, *Multidiscip. Model. Mater. Struct.*, 2006, **2**, p 363–387
15. M. Grujicic, B. Pandurangan, Y. Huang, B.A. Cheeseman, W.N. Roy, and R.R. Skaggs, Impulse Loading Resulting from Shallow Buried Explosives in Water-Saturated Sand, *J. Mater. Des. Appl.*, 2007, **221**, p 21–35
16. M. Grujicic, B. Pandurangan, G.M. Mocko, S.T. Hung, B.A. Cheeseman, W.N. Roy, and R.R. Skaggs, A Combined Multi-Material Euler/Lagrange Computational Analysis of Blast Loading Resulting from Detonation of Buried Landmines, *Multidiscip. Model. Mater. Struct.*, 2008, **4**, p 105–124
17. M. Grujicic, B. Pandurangan, R. Qiao, B.A. Cheeseman, W.N. Roy, R.R. Skaggs, and R. Gupta, Parameterization of the Porous-Material Model for Sand with Different Levels of Water Saturation, *Soil Dyn. Earthq. Eng.*, 2008, **28**, p 20–35
18. J. Foedinger, Methodology for Improved Characterization of Landmine Explosions, *SBIR Phase-II Plus Program, Technical Interchange Meeting*, Material Science Corporation, June 2005
19. R.R. Skaggs, J. Watson, T. Adkins, W. Gault, A. Canami, and A.D. Gupta, "Blast Loading Measurements by the Vertical Impulse Measurement Fixture (VIMF)," ARL Technical Report-3383, US Army Research Laboratory, Aberdeen Proving Ground, MD, 2005
20. M. Grujicic, W.C. Bell, G. Arakere, and I. Haque, Finite Element Analysis of the Effect of Up-Armoring on the Off-Road Braking and Sharp-Turn Performance of a High-Mobility Multi-Purpose Wheeled Vehicle (HMMWV), *J. Automob. Eng.*, 2009, **223**(11), p 1419–1434
21. M. Grujicic, G. Arakere, H.K. Nallagatla, W.C. Bell, and I. Haque, Computational Investigation of Blast Survivability and Off-Road Performance of an Up-Armored High-Mobility Multi-Purpose Wheeled Vehicle (HMMWV), *J. Automob. Eng.*, 2009, **223**, p 301–325
22. M. Grujicic, G. Arakere, W.C. Bell, and I. Haque, Computational Investigation of the Effect of Up-Armoring on Occupant Injury/Fatality Reduction of a Prototypical High-Mobility Multi-Purpose Wheeled Vehicle Subjected to Mine-Blast, *J. Automob. Eng.*, 2009, **223**, p 903–920
23. M. Grujicic, H. Marvi, G. Arakere, W.C. Bell, and I. Haque, The Effect of Up-Armoring the High-Mobility Multi-Purpose Wheeled Vehicle (HMMWV) on the Off-Road Vehicle Performance, *Multidiscip. Model. Mater. Struct.*, 2010, **6**(2), p 229–256
24. V.M.H. Sadd, DEM Simulation of Wave Propagation in Granular Materials, *Powder Technol.*, 2000, **109**, p 222–233
25. J. Dvorkin, A. Nur, and H. Yin, Effective Properties of Cemented Granular Materials, *Mech. Mater.*, 1994, **18**, p 351–366
26. V.S. Deshpande, R.M. McMeeking, H.N.G. Wadley, and A.G. Evans, Constitutive Model for Predicting Dynamic Interactions Between Soil Ejecta and Structural Panels, *J. Mech. Phys. Solids*, 2009, **57**, p 1139–1164
27. ANSYS/Autodyn-2D and 3D, *Version 11*, *User Documentation*, Ansys Inc., 2007
28. S. Stein and T. Kim, Effect of Moisture on Attraction Force on Beach Sand, *Mar. Geosour. Geotechnol.*, 2004, **22**, p 33–47
29. ABAQUS Version 6.9.1, *User Documentation*, Dassault Systems Inc., 2009
30. L.C. Taylor, W.L. Fourney, U. Leiste, and B.A. Cheeseman, Loading Mechanisms on a Target From Detonation of a Buried Charge, *24th International Symposium on Ballistics*, Vol 1, New Orleans, 2008
31. L.C. Taylor, W.L. Fourney, and U. Leiste, "Pressures on Targets From Buried Explosions," ARO STIR Final Report, 2010
32. HyperMesh 10.0, *Theory Manual*, Altair Engineering Inc., 2010
33. E.L. Lee, H.C. Hornig, and J.W. Kury, "Adiabatic Expansion of High Explosive Detonation Products," UCRL-50422, Lawrence Radiation Laboratory, University of California, 1968
34. M. Grujicic, B. Pandurangan, U. Zecevic, K.L. Koudela, and B.A. Cheeseman, Ballistic Performance of Alumina/S-2 Glass Fiber-Reinforced Polymer-Matrix Composite Hybrid Light Weight Armor Against Armor Piercing (AP) and Non-AP Projectiles, *Multidiscip. Model. Mater. Struct.*, 2007, **3**, p 287–312